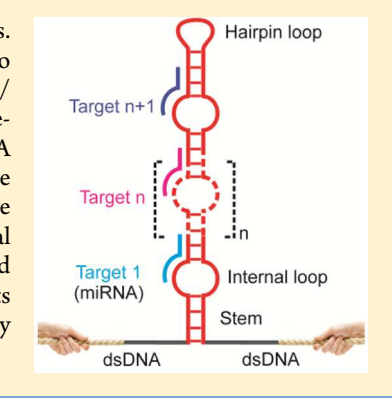


Single-Molecule Topochemical Analyses for Large-Scale **Multiplexing Tasks**

Shankar Mandal, * Xiaoqing Zhang, * Shankar Pandey, * and Hanbin Mao*, * Dankar Pandey, * D

Supporting Information

ABSTRACT: Multitasking is the pivotal feature in next-generation chemo- or bioanalyses. However, simultaneous analyses rarely exceed over three different tasks, which is ascribed to the limited space to accommodate analyzing units and the compromised signal-to-noise (S/ N) level as the number of tasks increases. Here, by leveraging superior S/N of singlemolecule techniques, we analyzed five microRNA biomarkers by spatially encoding miRNA recognition units with nanometers resolution in a DNA template, while decoding the analyte binding temporally in seconds. The hairpin stem is interspersed by internal loops to encode recognition units for miRNA. By mechanical unfolding of the hairpin, individual internal loops are sequentially interrogated for the binding of each miRNA. Using this so-called topochemical spatiotemporal analysis, we were able to achieve subpicomolar detection limits of miRNAs. We anticipate that this new single-molecule topochemical analysis can massively analyze single-molecule targets.



Rapid development of the Internet of Things (IOT)¹ calls for analytical devices with multiplexing capabilities to collect and analyze electrical, chemical, or biological signals from targets.2 In line with this growing demand, nextgeneration chemo- and bioanalyses require the capability to process a large scale of targets. For example, in the emerging lab-on-a-molecule field, multiple chemicals or ions are analyzed on a molecular template.³⁻⁵ However, constrained space in a template sets an upper limit of three analyzing units.⁵ In addition, as the number of analytes grows, ensemble signals become crowded and indistinguishable from each other due to signal-to-noise (S/N) issues. Compared to ensemble approaches, single-molecule methods provide superior S/N to analyze samples with low concentrations.

In single-molecule sensing, the ultimate mass detection limit of individual molecules can be reached. However, multiplex analyses of different analytes are often limited in singlemolecule methods using AFM⁶⁻⁹ or an optical tweezers¹⁰⁻ technique, in which molecules are processed one at a time. Parallel processing of many single-molecule templates can be achieved by magnetic tweezers 13-15 or fluorescence microscopy. 16-19 In these methods, encoding of different recognition units and decoding of the corresponding binding events become challenging. To address these coding problems, substrate surfaces in magnetic tweezers or fluorescence microscopies can be patterned so that each region hosts only one particular analyte. However, involved steps are necessary for surface patterning, which also suffers from a limited number of different analytes that can be accommodated in a typical pattern with micrometer resolutions (microchips^{20,21}).

Recently, we exploited an alternative approach to increase the multiplexing capacity in single-molecule analyses. 22 In this so-called single-molecule mechanochemical sensing method, we expanded the size of a template capable of incorporating multiple sensing units. For example, we used DNA origami nanoassembly as the sensing backbone.²² Not only can multiple recognition elements be encoded in the DNA origami, the binding events can also be differentiated (or decoded) by leveraging the 3D configuration of the origami structure. Since such a coding strategy utilizes the space of the sensing template, it has limited multiplexing capability as the size of the template becomes a bottleneck when the number of analytes increases.

To achieve large-scale multiplexing tasks, highly efficient coding approaches are therefore critical. As discussed above, current strategies suffer from limited space that can be exploited for both encoding and decoding of different analytes. We rationalize that, by performing encoding/decoding in both space and time, unlimited multiplex tasks can be achieved. To demonstrate this goal, we incorporated many recognition units with ~ 10 nm spacing in a DNA hairpin that is interspersed with internal loops. ^{23,24} During mechanical unzipping of the hairpin, each internal loop induces a transient drop in the unzipping force, partitioning the unzipping process into discrete steps. Due to the sequential unzipping nature of the hairpin that propagates from the base of the stem to the loop, the resultant sawtooth unzipping force pattern allows us to

Received: May 29, 2019 Accepted: September 25, 2019 Published: September 25, 2019



[†]Department of Chemistry and Biochemistry, Kent State University, Kent, Ohio 44242, United States

^{*}Key Laboratory of Clinical Laboratory Diagnostics (Ministry of Education of China), School of Laboratory Medicine, Chongging Medical University, Chongqing, 400016, People's Republic of China

differentiate individual internal loops that encode specific recognition units for analytes. Decoding is achieved by varied size or different stabilities of the fully addressed recognition units during their mechanical unfolding, which reveals the binding status of each analyte. Since both encoding and decoding exploit the topological arrangement of recognition units, we named our approach as single-molecule topochemical analysis, a term closely related to the topochemistry, which investigates localized chemical reactions under the influence of the topology of the reaction environment. As a proof of concept, we demonstrated that such a spatiotemporal coding scheme was able to specifically detect five different miRNAs with detection limits on the order of 100 fM in buffer and 1 pM in 10× diluted serum within 25 min. Since any number of internal loops can be prepared with a fully addressable fashion based on the location and sequential arrangement of internal loops, such a spatiotemporal coding system can readily characterize massive number of different analyte molecules.

EXPERIMENTAL SECTION

Materials and Reagents. All DNA oligomers were purchased from Integrated DNA Technologies (www.idtdna. com) and purified with denaturing polyacrylamide gel electrophoresis (PAGE). HPLC-purified miRNA 151 and miRNA let 7a were purchased from Integrated DNA Technologies (www.idtdna.com). The miRNA 369, miRNA 21, and miRNA 222 were synthesized using a MEGAscript T7 Transcription Kit (www.thermofisher.com). All chemicals, including Tris-HCl, KCl, EDTA, and DEPC, were purchased from either Fisher Scientific or Sigma with purities >99.0%. Unless specified otherwise, all enzymes were obtained from New England Biolabs (www.neb.com). The streptavidin or antidigoxigenin antibody coated polystyrene beads for laser tweezers experiments were purchased from Spherotech (Lake Forest, Illinois, U.S.A.). Human serum and bovine serum albumin (BSA, >98.0%) were purchased from Germini (West Sacramento, CA) and Amresco (Solon, Ohio, U.S.A.), respectively.

Synthesis of the DNA Constructs Used in Single-Molecule Topochemical Experiments. The DNA construct for single-molecule topochemical sensing of nucleic acid fragments (DNA/miRNA; Table S1) was prepared by sandwiching a DNA hairpin between 2028 and 2690 bp DNA handles. The DNA hairpin contains multiple internal loops and stems as analyte recognition and signal reporting units for multiplex topochemical sensing of miRNAs (Figure S1). The 2690 bp dsDNA handle was synthesized by SacI (NEB) and EagI (NEB) digestions of a pEGFP plasmid (Clontech, Mountain View, CA). The digested 2690 bp handle was gel purified using a kit (Midsci, St. Louis, MO). The handle was subsequently labeled at the 3' end by digoxigenin (Dig) using 18 µM Dig-dUTP (Roche, Indianapolis, IN) and terminal transferase (Fermentas, Glen Burnie, MD). The biotin-labeled 2028 bp dsDNA handle was prepared by PCR amplification of pBR322 plasmid (New England Biolab, NEB) using a 5' biotinylated reverse primer (IDT, Coralville, IA). The PCR product was purified with QIAquick PCR purification kit (Qiagen, Germantown, MD) and subsequently digested with XbaI restriction enzyme (NEB). The digested 2028 bp handle was gel purified using a QIAquick gel extraction kit (Qiagen, Germantown, MD).

Different DNA constructs were synthesized by stepwise ligation of different DNA oligomers (Table S2) with two long

dsDNA handles (2028 bp and 2690 bp) using T4 DNA ligase (NEB; see the schemes in Figure S1). In general, to synthesize the DNA construct 1 (Figure S1A), an oligonucleotide 5' CTAG TG CAT TAG GAA GCA GCC CAG TAG TAG GAA AAA AAA GAT CG AAC TAT ACA AC C TAC TAC CTC A 3' (Oligo-1), which contained 11-nt toehold to bind with miRNA let 7a (Table S1), and a part of the hairpin stem (11 bp, underlined) was annealed with an oligonucleotide 5' TTT TTT TTC CTA CTA CTG GGC TGC TTC CTA ATG CA 3' (Oligo-2) at 97 °C for 5 min and slowly cooled to room temperature for 2 h. This fragment was ligated with the 2028 bp DNA handle by T4 DNA ligase (NEB) and gel purified using a QIAquick gel extraction kit (Qiagen, Germantown, MD). On the other side of the DNA construct, oligonucleotides 5' GGAC T GAG GTA GTA G CA ACA TAT CAA GC TAG GCC AGC AAG ACG TAG CCC AGC GCG TC 3' (Oligo-3) containing another part of the hairpin stem (15 bp, underlined) was annealed with oligonucleotides, 5' GGCC GAC GCG CTG GGC TAC GTC TTG CTG GC 3' (Oligo-4). This fragment was ligated with the 2690 bp handle and gel purified. The final DNA construct was synthesized using T4 DNA ligase (NEB) through three-piece ligation of the 2028 and 2690 bp DNA handles and an ssDNA fragment, 5' GTC CGG ACC CTG TTTT CAG GGT CC 3'(Oligo-5), which contained a tetra thymine loop with underlined regions representing the complementary regions of the hairpin stem. To prepare DNA constructs 2, 3, and 4 (Figure S1B-D), the 2028-bp and 2690-bp handles were synthesized using a similar strategy described above by employing oligonucleotides listed in Table S2. The final DNA constructs 2, 3, and 4 were ligated after self-assembly of appropriate DNA oligomers listed in Table S2 according to the schemes shown in Figure S1B-D. The DNA construct for large-scale target analyses (Figure 6) was synthesized according to the scheme described in Figure

Preparation of Four-Channel Microfluidic Chambers. The single-molecule mechanochemical studies were performed in a four-channel microfluidic chamber in laser tweezers instrument. CorelDraw program (Corel Corporation, Ottawa, Canada) was used to prepare microfluidic patterns (Figure S2) and imprinted into the Para-film (BEMIS, Neenah, WI) on a glass coverslip by a laser cutter (VL-200, Universal Laser Systems, Scottsdale, AZ). The imprinted para-film was thermally sealed at 85 °C between two #1 VWR glass coverslips. Two microcapillary tubes (ID 25 μ m, OD 100 μ m, King Precision Glass, Inc. California) were used to make an internal conduit between middle channels and the top and bottom channels to transport digoxigenin-antibody- and streptavidin-coated beads into the buffer and target channels, respectively. The single-molecule topochemical experiments were performed in the middle of the buffer and the target channels to avoid the variation of flow rates from the edge effects. The distance between the buffer and the target channels through the conduit was about 500 μ m (see Figure

Single-Molecule Topochemical Experiments. The single-molecule topochemical experiments were performed in the four-channel microfluidic chamber (Figure S2) in laser tweezers instrument. The detailed description of the laser tweezers instrument and methods used for the single-molecule experiments have been reported elsewhere. Briefly, to perform single-molecule experiment, diluted DNA construct (\sim 1 ng) was incubated with 1 μ L of 0.1% solution of

digoxigenin (Dig)-antibody coated polystyrene beads (diameter: 2.10 μ m) for about 30 min at room temperature (25 °C), which immobilized the Dig-labeled DNA construct on the bead surface through Dig-anti-Dig complex formation. The incubated sample was further diluted to 1 mL in a 10 mM Tris buffer (pH 7.4, supplemented with 100 mM KCl). Streptavidin-coated polystyrene beads (1 μ L, diameter: 1.87 um) were also dispersed into the same buffer (1 mL) and injected into the microfluidic chamber (Figure S2). A 10 mM Tris buffer (pH 7.4) containing 100 mM KCl, 1× BSA, and RNase inhibitors (Murine; www.neb.com) without and with target miRNA was flowed in the top (buffer) and bottom (target) channels, respectively. The streptavidin-coated bead was trapped in the target channel and moved to the buffer channel where the antibody-coated bead was trapped by another laser beam. The DNA construct initially on the surface of the antibody-coated bead was tethered between the two types of the beads in the buffer channel by escorting one of the beads closer to another using a steerable mirror (Madcity Laboratories Inc., Madison, WI). In the ramping-force detection mode (F-X mode), the antibody-coated bead was moved away from the streptavidin-coated bead with a loading speed of \sim 5.5 pN/s by using the steerable mirror. The hairpin structure was unfolded when the tension inside the tether was gradually increased. The unfolding of the hairpin structure was depicted by a sudden change in the end-to-end distance during the process. Single-molecule tether was confirmed by a DNA overstretching plateau at 65 pN or a single-step breakage event in the force-extension (F-X) curves. The F-X curve for each tether was recorded in a Labview 8 program (National Instruments Corp., Austin, TX), and data treatment was performed using Matlab (The MathWorks, Natick, MA) and Igor (WaveMetrics, OR, U.S.A.) programs. The unfolding force was measured directly from the F-X curves, while the change-in-contour-length (ΔL) due to the unfolding was calculated by the two data points flanking a rupture event using an extensible worm-like chain (WLC) model (eq 1)^{26,2}

$$\frac{\Delta x}{\Delta L} = 1 - \frac{1}{2} \left(\frac{k_{\rm B} T}{FP} \right)^{1/2} + \frac{F}{S} \tag{1}$$

where Δx is the change in extension between the data points of the stretching and relaxing curves at the same force (F), $k_{\rm B}$ is the Boltzmann constant, T is absolute temperature, P is the persistent length $(50.8 \pm 1.5 \text{ nm})$, 28 F is the force, and S is the elastic stretch modulus $(1243 \pm 63 \text{ pN})$.

RESULTS AND DISCUSSION

Strategy of Single-Molecule Mechanochemical Sensing for Nucleic Acid Fragment. Single-molecule mechanochemical biosensor to detect miRNA in a laser tweezers setup is shown in Figure 1. The sensor consists of a DNA hairpin juxtaposed by an ssDNA segment. The sensing probe is sandwiched between two long dsDNA handles (Figures 1A and S1A), which are tethered to two optically trapped beads via affinity linkages for mechanical unfolding and refolding of the single-molecule sensor in laser tweezers. The ssDNA serves as a toehold^{29,30} recognition site, whereas the DNA hairpin functions as both the receptor and the signal reporter for the binding of complementary miRNA target(Figure 1A). Target binding to the ssDNA toehold region leads to partial unfolding of the hairpin, which causes a smaller change-in-contour-length (ΔL) or decreased unfolding force compared to the control

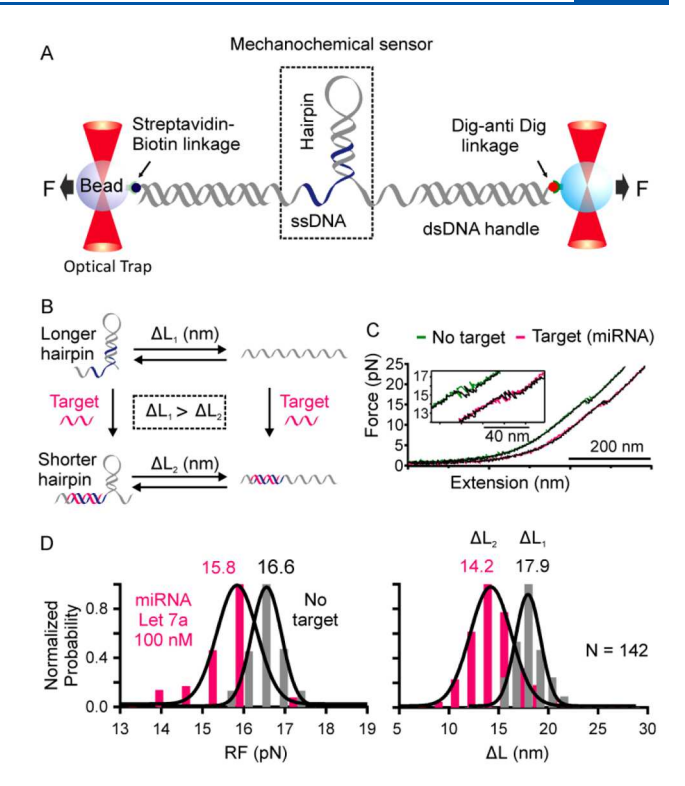


Figure 1. One-tiered mechanochemical analysis of a single miRNA molecule in laser tweezers. (A) A single-molecule mechanochemical sensing construct consists of a DNA hairpin flanked by a single-stranded DNA, which is sandwiched between two long dsDNA handles. (B) The miRNA target first binds to the ssDNA toehold region and invades to the DNA hairpin stem (blue). After mechanical unfolding, the target bound DNA hairpin shows smaller change-in-contour-length (ΔL ; bottom right) compared to the free DNA probe (top right, see Figure S3 for detailed calculation). (C) Representative F-X curves of the DNA construct in the Tris buffer without (green) and with (pink) 100 nM miRNA Let 7a. (D) The RF and ΔL histograms of the DNA construct in the Tris buffer without (gray) and with (pink) 100 nM miRNA Let7a.

DNA construct without target (Figure 1B, see Figure S3 for ΔL comparison).

To characterize the single-molecule mechanochemical sensor, we first performed force-ramping experiments on the sensor in a 10 mM Tris buffer (pH 7.4) with 100 mM KCl at room temperature without and with 100 nM miRNA Let 7a³¹ (Figure 1C, see Table S1 for the sequence) in a four-channel microfluidic chamber in a laser tweezers instrument (Figure S2). The force-extension (F-X) curves clearly showed that the target-bound DNA hairpin was unfolded at lower force with a smaller step size compared to the control DNA hairpin (Figure 1C, inset). To determine the nature of these unfolding transitions, we analyzed the change-in-contour-length (ΔL) and the rupture force (RF) of the hairpin mechanophore with and without target miRNA (Figure 1D and eq 1 in the Experimental Section). The observed ΔL (14.2 \pm 0.3 nm) and RF (15.8 \pm 0.1 pN; Figure 1D, pink) for target-bound DNA hairpin were lower compared to those for free DNA hairpin $(\Delta L: 17.9 \pm 0.2 \text{ nm}; \text{RF}: 16.6 \pm 0.1 \text{ pN}; \text{Figure 1D, gray}). \text{ The}$ decrease in the ΔL value was expected by theoretical calculations (see eq S1 in the Supporting Information and Figure S3), whereas the decrease in RF is due to the shorter stem size of the hairpin³² upon binding of the miRNA target.

It is clear from Figure 1D that, in 100 nM miRNA target concentration, the RF and ΔL histograms for target and control have some overlaps. These problems may be solved by optimizing the stem length of the DNA hairpin. For an example, the length of the DNA stem can be made shorter than miRNA sequence so that the latter can effectively invade through the entire DNA stem due to increased thermodynamic stability. This will dissolve the hairpin to generate distinct histogram patterns with and without targets. To determine the limit of detection (LOD) of the miRNA target using current sensing template, we compared RF versus ΔL plots of individual F-X traces from the same sensing molecule with and without targets (Figure 2). First, we obtained more than

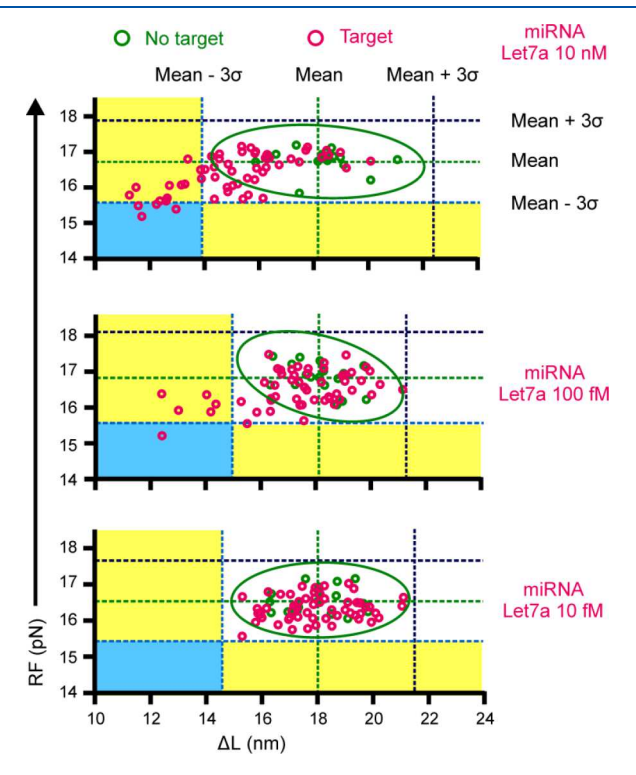


Figure 2. Rupture force (RF) vs change-in-contour-length (ΔL) plots of the unfolding event in each F-X curve to determine the limit of detection (LOD) of Let 7a miRNA. Green ellipses indicate the data range of 95% confidence level in the buffer channel.

15 ΔL and RF measurements of a sensor in the buffer channel to calculate average $\Delta L_{\rm avg}$ and RF_{avg} with standard deviations (σ). The same DNA sensor was then transported to the miRNA channel with specific concentrations to collect 50 F-X traces for about 25 min. Binding of the miRNA was depicted by decreased values (3σ) of either ΔL or RF, or both, with respect to $\Delta L_{\rm avg}$ or RF_{avg} (Figure 2, yellow region, 99.7% confidence level). Compared to ΔL , the RF was not as sensitive to report the binding of miRNA. After evaluating the ΔL -RF plots at different miRNA concentrations (see 100 and 10 fM in Figure 2, for example), we found Let 7a miRNA had a LOD of 100 fM in 25 min (\geq 50% detection probability, $n \geq$ 4). Further concentration decreases to 10 fM did not yield binding events (Figure 2, bottom panel).

Single-Molecule Mechanochemical Sensing for Multiplexing Tasks. To demonstrate multiplex tasking of the mechanochemical sensor, we incorporated a symmetrical internal loop in the DNA hairpin probe (Figure 3A). The

internal loop contains 21 mismatch base pairs, which separate the hairpin into two stems of 23 (stem 1) and 25 (stem 2) bp in length (see Figure S1C for details). The size of the internal loop (21 nt) was determined by the best binding efficiency between the 22-nt ssDNA (DNA Let 7a, see Table S1), a surrogate for miRNA Let 7a (Table S1), and a 11-nt toehold^{29,30} region in DNA loops of different sizes (11, 22, or 33 nt, see Figures S1B and S4).

Specific miRNA targets first partially hybridize with the 11nt toehold either in the flanking ssDNA or the internal loop (Figure 3A). This is followed by a full hybridization to the duplex hairpin stem (~11 bp) by displacing one of the complementary strands. As a result, the remaining hairpin becomes weakened, reducing both rupture force (RF) and ΔL (Figure 3A, right). Sensing experiments confirmed these expected patterns. Mechanical unfolding of the free mechanochemical sensor produced two features. While the first feature corresponds to the unfolding of the stem 1 and the internal loop, the second feature is for the unfolding of the stem 2 and the hairpin loop (Figure 3B, middle, yellow background). Binding of either 50 nM target 1 (miRNA 369)³³ or target 2 (miRNA Let 7a)³¹ reduced the RF and ΔL of the first feature only (Figure 3B,C, Tier 1), whereas binding of 50 nM target 3 (miRNA 151)³⁴ reduced RF and ΔL of the second feature only (Figure 3B,C, Tier 2).

In the presence of all three targets, 1, 2, and 3, the first feature disappeared due to the binding of targets 1 and 2, while the second feature had smaller RF and ΔL due to the target 3 binding. During binary target binding, targets 1 and 2 led to the disappearance of the first feature, whereas the second feature was unaffected. In the presence of targets 1 and 3 or 2 and 3, both the first and the second features showed reduced RF and ΔL values (Figure 3B,C, see Tiers 1 and 2). These experiments clearly demonstrated that any combination of the three miRNA targets can be differentiated by this multitasking single-molecule sensor.

After specific recognition of the three miRNAs (Figure 3) at relatively high concentration (50 nM) using ΔL or RF histograms, next, we proceeded to determine the LOD of each miRNA. At rather low concentrations, most F-X curves did not show binding events, generating a histogram indistinguishable with that of the control without any targets. To address this issue, similar to Figure 2, RF versus ΔL plots of individual F-X curves with a higher signal-to-noise ratio were used for LOD determination.

To increase the confidence level, we also evaluated the recognition events at the 5σ levels (99.9% confidence level, see Figure 4). First, we obtained RF versus ΔL plots to identify positive target binding events using 50 nM miRNA targets. For miRNA target 1, most bound data were beyond 5σ of both $\Delta L_{
m avg}$ and RF $_{
m avg}$ from the first unfolding feature (Tier 1 detection), whereas they were located beyond 3σ for miRNA target 2 (Figure 4). In contrast, for miRNA target 3, bound features were concentrated beyond 3σ of $\Delta L_{\rm avg}$ for the second feature only (Figure 4, right). We therefore used these criteria as the thresholds in the multi-tiered detection schemes to identify binding events of specific miRNA at low concentration levels (see Figure 4 middle row for 100 fM miRNAs). We found LOD of 100 fM for each of the three miRNAs (miRNA 369, Let 7a, and 151) in the Tris buffer; and 1 pM (Figure 4, third row) in 10× diluted serum within a time window of 25 min (\geq 50% detection probability, $n \geq 4$).

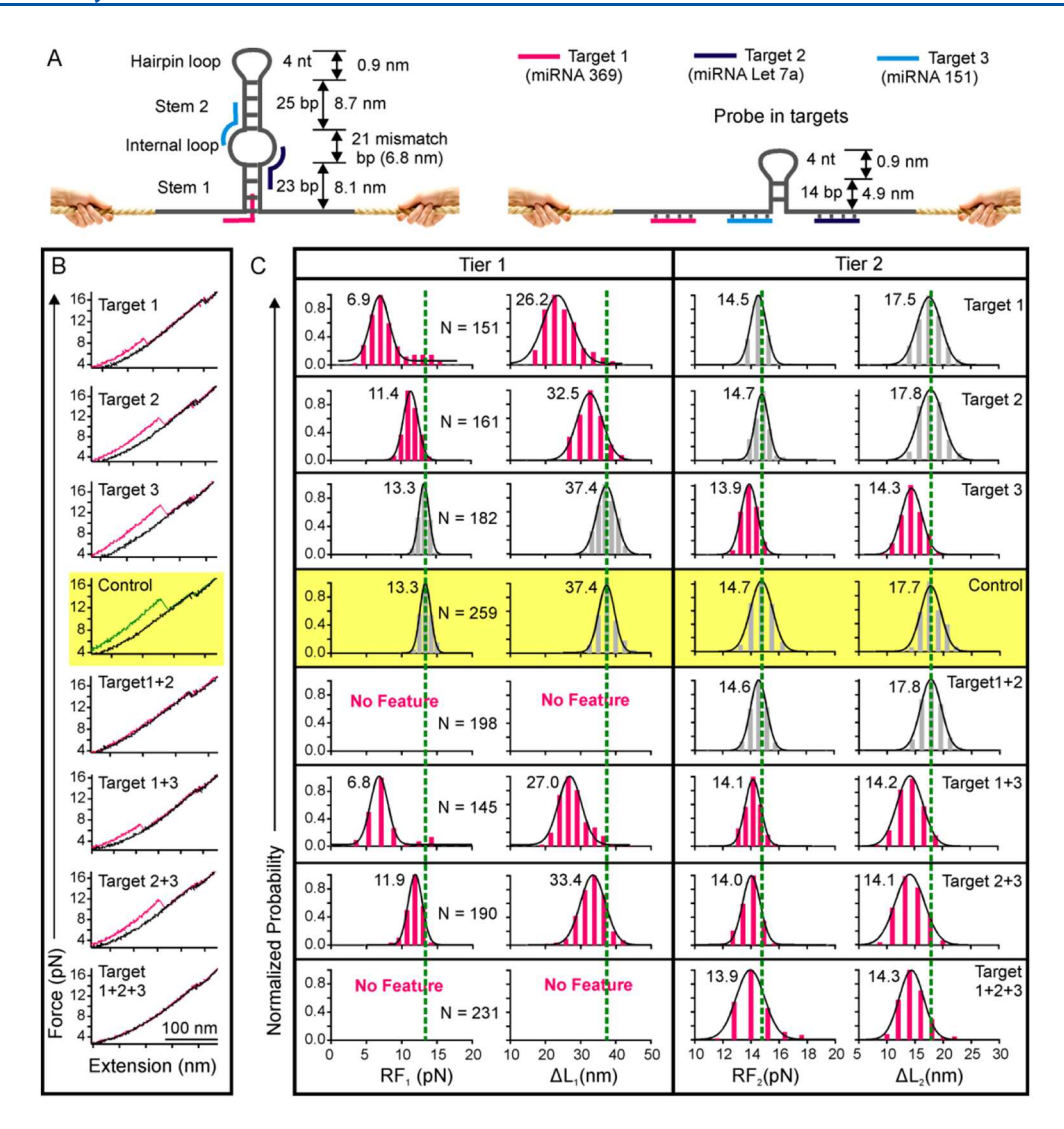


Figure 3. Two-tiered topochemical analyses of three miRNAs. (A) The probe consists of a DNA hairpin with a symmetrical internal loop and an adjacent ssDNA fragment serving as toeholds. Target 1 binds with the ssDNA toehold and invades into the stem 1. Targets 2 and 3 bind with the internal loop toeholds and then hybridize to the stems 1 and 2, respectively. Binding of all three targets destabilize the internal loop and both stems, yielding a much smaller hairpin structure (right). (B) Representative F-X curves of the DNA probe with (pink) and without (green) 50 nM miRNA targets in the 10 mM Tris buffer supplemented with 100 mM KCl at pH 7.4. Binding of targets reduces the change-in-contour-length (ΔL) and rupture force (RF) of the respective unfolding features. (C) The RF and ΔL histograms with (pink) and without (gray) 50 nM miRNA targets. Dotted green lines are the guides to the eye.

To evaluate the specificity of miRNA target binding, RF versus ΔL was also plotted at the second unfolding feature (Tier 2 detection) for miRNA 369 and Let 7a, as well as at the first unfolding feature (Tier 1 detection) for miRNA 151 in buffer and in 10× diluted serum (Figure S5). We did not observe any target binding event during Tier 2 detection for miRNA 369 and Let 7a or Tier 1 detection for miRNA 151 according to the criteria as discussed above, which indicates that the 2-tiered sensing probe can specifically bind with different miRNAs. The 100 fM LOD was also observed in any target combinations among the three miRNAs (see Figures S6 and S7). It is significant that these LODs are already lower than the natural miRNA concentration in human serum, 35,36 suggesting our single-molecule sensing can be directly applied for field samples. Based on the methods described in our previous report,³⁷ we expect that our topochemical sensor can differentiate single nucleotide polymorphism or variation (SNP or SNV). Indeed, when we evaluated the LODs of DNA

surrogates of microRNA Let 7a and Let 7c (5'-TGAGGTAG-TAGGTTGTAT \underline{G} GTT, underlined sequence depicts the SNV in the Let 7c;³⁸ Table S1) using the two-tiered sensor shown in Figures 3, we found that the Let7a has an LOD \sim 5 orders of magnitude lower than the Let 7c (Figure S8).

To quantify miRNAs using our topochemical approach, we constructed a calibration curve by plotting observation time for the first binding event against known concentrations of miRNA Let 7a. Immediately after the sensing probe was switched from the buffer channel to the target channel within 10 s, F-X curves were recorded at 20 s intervals. The time for miRNA binding was determined when either RF or ΔL of the hairpin reporter was smaller than $(RF_{avg} - 3\sigma)$ or $(\Delta L_{avg} - 3\sigma)$ (Figure 4). Using two-tiered topochemical sensing strategy (Figure 3), we obtained a linear range of 100 fM to 100 nM for miRNA Let 7a within a time window of ~25 min (Figure S9) in 10 mM Tris buffer (pH 7.4) supplemented with 100 mM KCl. From the first binding time of the target, the unknown

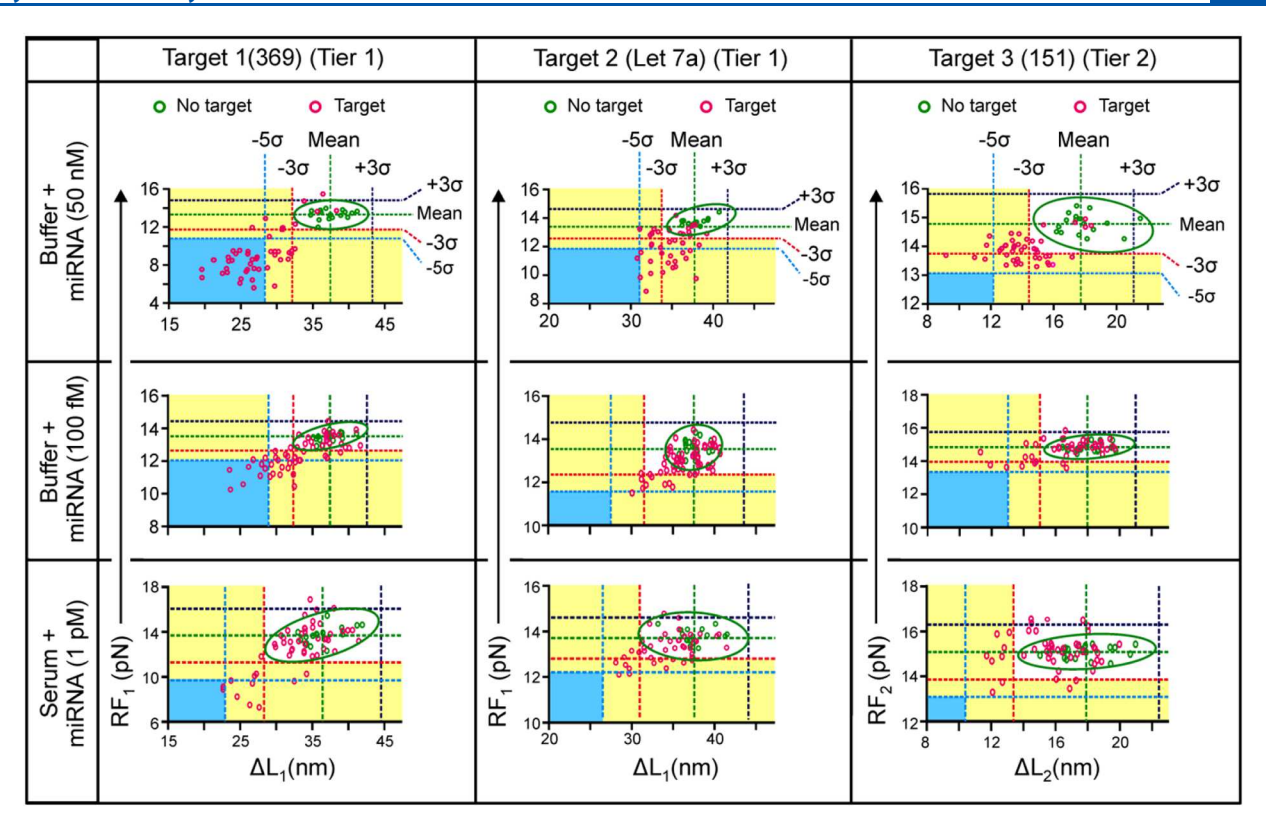


Figure 4. Pattern recognition in the two-tiered topochemical analyses for miRNAs. Binding of individual targets is recognized in the RF vs Δ L plot of either the 1st (Tier 1) or the 2nd (Tier 2) unfolding feature of individual F-X curves. Green and pink depict without and with miRNA targets, respectively. Ellipses indicate the data range at 95% confidence level without target.

concentration can be estimated from the calibration curve. Due to the similar binding time at specific concentration for different miRNAs used in this report (Table S3), we anticipate similar quantification ranges exist among different miRNAs.

Spatiotemporal Coding Capable of Large-Scale miRNA Analyses. With successful demonstration of multiplex sensing of three miRNA targets, we set out to explore the possibility of large-scale miRNA analyses. We used multiplex sensing of five miRNAs as a proof-of-concept. To this end, we expanded the spatiotemporal coding by introducing a total of four internal loops in the hairpin, which separate the hairpin stem into five regions (Figures 5A and S1D). Each internal loop serves as a separate toehold to initiate different miRNA binding. The probe also contains a flanking ssDNA in the hairpin base to serve as an additional toehold (Figure 5A). Without any target, the DNA probe is expected to produce five sawtooth unfolding signals corresponding to the sequential unfolding of five stems that are interrupted by the four internal loops (Figure 5A, top right). When Target 1 (miRNA 369)³³ is present, it first binds to the 11-nt ssDNA toehold via complementary base pairing, followed by invading into the stem 1 by 11-bp hybridization. The resultant stem 1 becomes shorter with decreased unfolding force and smaller ΔL (Figure 5A, bottom right). Similarly, for Targets 2–5 (miRNA 21, Let 7a, 222, and 151, respectively), 31,34,38,39 bindings start with the 11-nt toeholds in the internal loops 1-4, respectively, which are followed by the 11-bp hybridizations to the corresponding stems 2–5 (Figure 5A, left panel).

These predictions were exactly observed when 50 nM of individual miRNA targets were tested in the Tris buffer. While the F-X curve showed five distinctive unfolding features (Figure 5B, green) without targets, binding of target 1

(miRNA 369) reduced both the rupture force (RF) and the size (ΔL) of the stem 1 in the first unfolding feature (Figure 5B,C, pink). Likewise, binding of miRNA 21, miRNA Let 7a, miRNA 222, and miRNA 151 reduced the size (ΔL) of the stems 2, 3, 4, and 5, respectively (Figure 5B,C). Similar to previous probes, the decrease in the RF was not as significant as ΔL for these miRNA targets. When five miRNAs at 50 nM were tested together, each target was bound with the corresponding internal loop-stem region, producing expected ΔL signal in the five-tiered analyzing system (Figure 5C, bottom row). We anticipate that using the approach described in Figure 4, we could be able to detect all five miRNAs in fM concentrations.

CONCLUSIONS

As each specific transition event in the sawtooth unfolding pattern exactly corresponds to a particular recognition unit, such a single-molecule template contains probing units whose identities are fully addressed. Since the interaction of an analyzing unit and the corresponding analyte occurs at a particular location whereas their interaction status is probed according to their localized arrangement with respect to other interactions, we call this single-molecule method as topochemical analysis. This strategy avoids any ambiguity presented in conventional designs in which a signal variation may correspond to more than one analyte. For example, bindings of miRNA 369 and Let 7a cannot be differentiated at low concentrations by the design described in Figure 4. In current strategy, by interrogating characteristic ΔL features for the first and the third unfolding events (Figure 5A), bindings of these two miRNAs can be readily determined. Another

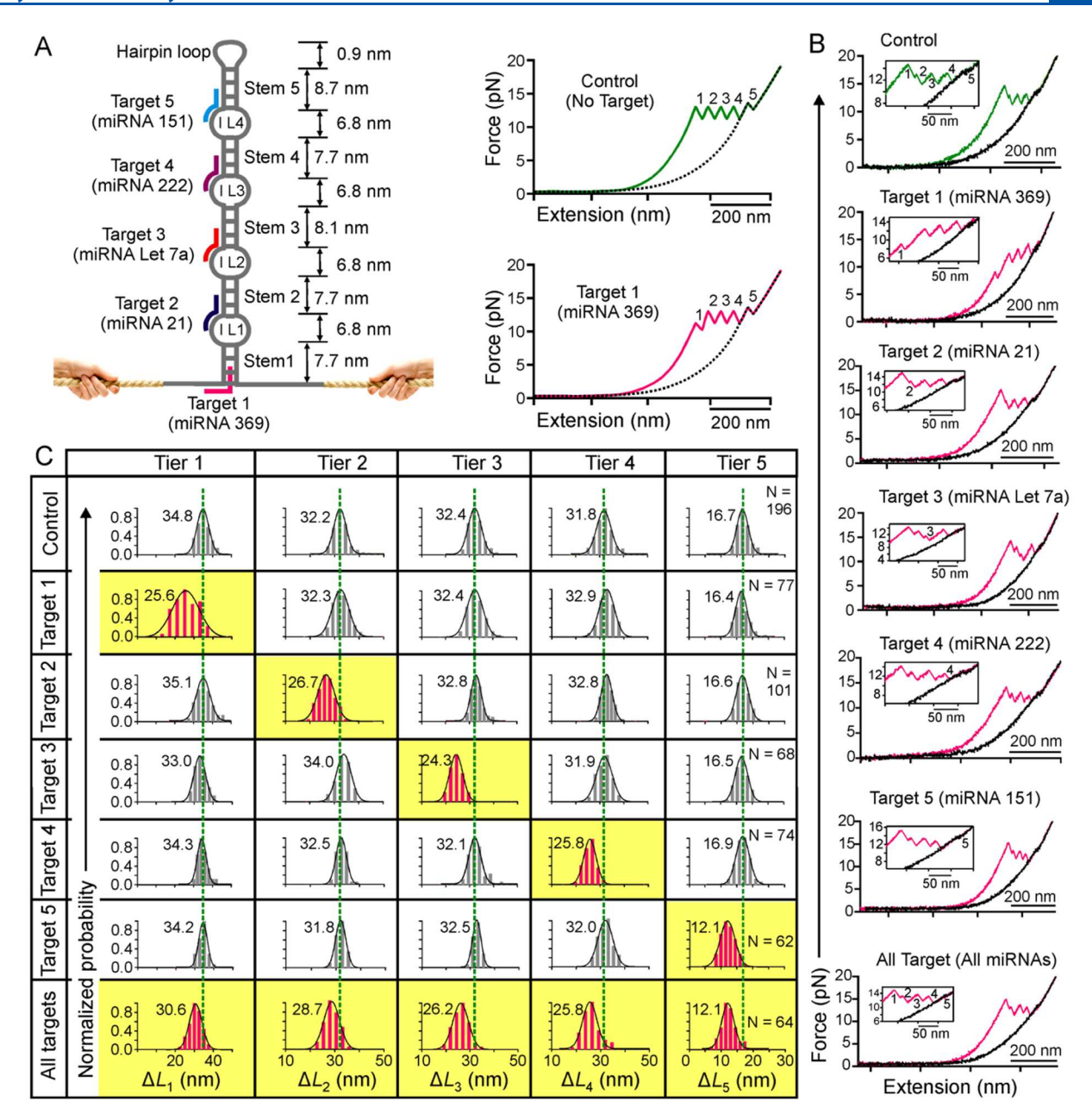


Figure 5. Single-molecule probe capable of large-scale topochemical analyses of miRNAs. (A) Schematic of the hairpin sensor that contains four internal loops (IL1-IL4) and five stems. Target 1 (pink) binds with the toehold at the base of the probe and invades into stem 1. Targets 2–5 bind with internal loop toeholds and half-length of the corresponding stems. Without target, the DNA construct produces five well addressed unfolding features (top right). With target 1, both RF and Δ L of the first feature are expected to be smaller (bottom right). Dotted curves depict relaxing F-X traces. Note feature 5 indicates the transition for the stem linked to the hairpin tetraloop. (B) Representative F-X curves of the probe without (green) and with (pink) 50 nM miRNAs in 10 mM Tris buffer (pH 7.4 with 100 mM KCl). (C) Change-in-contour-length (Δ L) histograms of a particular unfolding feature without (gray) and with (pink) 50 nM miRNA targets. Dotted green lines are the guides to the eye.

special feature of this spatiotemporal coding is its high density. Current design allows a spacing of ~ 10 nm between adjacent analyzing units. This spacing can be further reduced if the targets to be analyzed are small molecules, instead of nucleic acids that require relatively bulky toehold or hybridization regions. ^{29,30} In the case that aptamer probes ^{40,41} are used for small molecule analytes, ~ 5 nm/unit coding density is expected to be achieved. For a hairpin made of lambda DNA (48.5 kbp), ⁴² for example, this suggests ~ 3000 analyzing units can be incorporated for target analyses. Further increase in the unit number can be achieved readily with molecular biology

approaches to generate longer templates. It is significant that the spatial resolution in this spatiotemporal coding well exceeds that of super-resolution fluorescence microscopy. ^{16–19} Such small spacing between analyzing units is already equivalent to the smallest transistors incorporated in the silicon wafer by the most advanced lithography nowadays. ⁴³ However, to reach the reading and writing efficiency of the microelectronics, the temporal resolution in the decoding needs to be improved, which can be partially achieved by increasing the pulling speed for the hairpin probe.

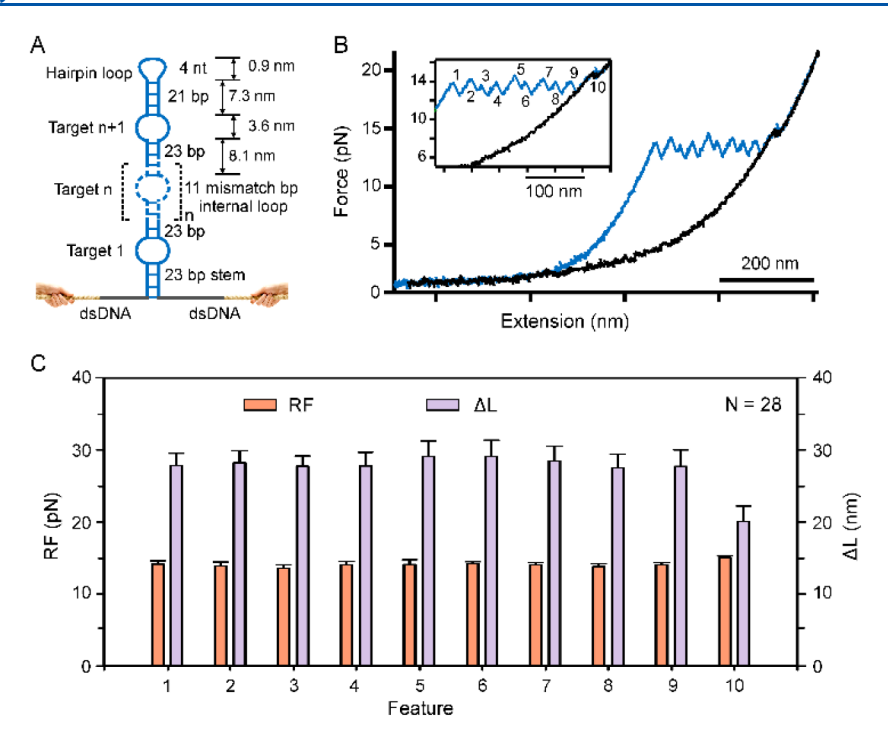


Figure 6. Single-molecule probe capable of massive multiplex evaluation of targets. (A) Schematic of the single-molecule topochemical probe consisting of n recognition units. (B) Representative F-X curves in 10 mM Tris pH 7.4 supplemented with 100 mM KCl showed sawtooth unfolding features correspond to ten recognition units. (C) The RF and ΔL diagrams [mean \pm SD, N = 28]. The observed ΔL for different unfolding features is close to the theoretical ΔL , as calculated by eq S1 (see SI, Material and Methods).

By adopting a coding strategy that exploits both space and time to differentiate analytes, we have successfully demonstrated a single-molecule topochemical platform capable of massive analyses of different single-molecules (single-molecule topochemical analyses). The spatiotemporal coding principle used here is generic. It can be readily extended to analyze massive number of single-molecule targets. For example, by using molecular biology methods, hairpins can be easily prepared with a large set of internal loops each serving as a recognition element (spatial encoding; see Figure 6 for a DNA construct with 10 recognition elements; see Figure S10 for its sequence and synthesis). The analyte binding is then decoded by mechanical unfolding events that are sequential in time (temporal decoding). When the internal loops are replaced by aptamers, analyses of a massive number of small-molecules or macromolecules can be accomplished. The spatiotemporal coding can also be used for the massive screening of bioactive chemicals if the internal loops are replaced by peptides or biomolecules other than nucleic acids.

ASSOCIATED CONTENT

S Supporting Information

The Supporting Information is available free of charge on the ACS Publications website at DOI: 10.1021/acs.analchem.9b02483.

Synthesis of miRNAs, calculation of change-in-contourlength (ΔL) and probe density, Tables S1–S3, and Figures S1–S10 (PDF)

AUTHOR INFORMATION

Corresponding Author

*E-mail: hmao@kent.edu.

ORCID ®

Shankar Mandal: 0000-0002-2653-8760 Hanbin Mao: 0000-0002-6720-9429

Author Contributions

The manuscript was written through contributions of all authors.

Notes

The authors declare no competing financial interest.

ACKNOWLEDGMENTS

H.M. thanks financial support from National Science Foundation [CHE-1609514], National Science Foundation [NSF (CBET1904921)] and National Institutes of Health [NIH 1R01CA236350] (in part).

REFERENCES

- (1) Atzori, L.; Iera, A.; Morabito, G. Comput. Netw. 2010, 54 (15), 2787–2805.
- (2) Gubbi, J.; Buyya, R.; Marusic, S.; Palaniswami, M. Future Gener. Comput. Syst. 2013, 29 (7), 1645–1660.
- (3) Magri, D. C.; Brown, G. J.; McClean, G. D.; de Silva, A. P. J. Am. Chem. Soc. **2006**, 128 (15), 4950–4951.
- (4) Magri, D. C.; Camilleri Fava, M.; Mallia, C. J. Chem. Commun. **2014**, 50 (8), 1009–1011.
- (5) Chen, K.; Shu, Q.; Schmittel, M. Chem. Soc. Rev. 2015, 44 (1), 136–160.
- (6) Rief, M.; Gautel, M.; Oesterhelt, F.; Fernandez, J. M.; Gaub, H. E. Science 1997, 276 (5315), 1109–12.
- Oberhauser, A. F.; Marszalek, P. E.; Erickson, H. P.; Fernandez,
 M. Nature 1998, 393 (6681), 181–5.
- (8) Florin, E.; Moy, V.; Gaub, H. Science 1994, 264 (5157), 415-417.
- (9) Moy, V.; Florin, E.; Gaub, H. Science 1994, 266 (5183), 257-259.

(10) Ashkin, A.; Dziedzic, J. M.; Bjorkholm, J. E.; Chu, S. Opt. Lett. 1986, 11 (5), 288–290.

- (11) Smith, S. B.; Cui, Y. J.; Bustamante, C. Science 1996, 271 (5250), 795-799.
- (12) Svoboda, K.; Schmidt, C. F.; Schnapp, B. J.; Block, S. M. Nature 1993, 365, 721.
- (13) Smith, S. B.; Finzi, L.; Bustamante, C. Science 1992, 258, 1122–1126.
- (14) Assi, F.; Jenks, R.; Yang, J.; Love, C.; Prentiss, M. J. Appl. Phys. **2002**, 92 (9), 5584–5586.
- (15) Ribeck, N.; Saleh, O. A. Rev. Sci. Instrum. 2008, 79 (9), 094301.
- (16) Dickson, R. M.; Cubitt, A. B.; Tsien, R. Y.; Moerner, W. E. *Nature* **1997**, 388, 355.
- (17) Betzig, E.; Chichester, R. J. Science 1993, 262 (5138), 1422-1425.
- (18) Hell, S. W.; Wichmann, J. Opt. Lett. 1994, 19 (11), 780-782.
- (19) Rust, M. J.; Bates, M.; Zhuang, X. Nat. Methods 2006, 3, 793.
- (20) Proudnikov, D.; Timofeev, E.; Mirzabekov, A. Anal. Biochem. **1998**, 259 (1), 34–41.
- (21) Arenkov, P.; Kukhtin, A.; Gemmell, A.; Voloshchuk, S.; Chupeeva, V.; Mirzabekov, A. *Anal. Biochem.* **2000**, 278 (2), 123–131.
- (22) Koirala, D.; Shrestha, P.; Emura, T.; Hidaka, K.; Mandal, S.; Endo, M.; Sugiyama, H.; Mao, H. *Angew. Chem., Int. Ed.* **2014**, *53*, 8137–8141.
- (23) Kahn, J. D.; Yun, E.; Crothers, D. M. Nature 1994, 368 (6467), 163–166.
- (24) Prislan, I.; Lee, H.-T.; Lee, C.; Marky, L. A. J. Phys. Chem. B **2015**, 119 (1), 96–104.
- (25) Mao, H.; Luchette, P. Sens. Actuators, B 2008, 129, 764-771.
- (26) Baumann, C. G.; Smith, S. B.; Bloomfield, V. A.; Bustamante, C. Proc. Natl. Acad. Sci. U. S. A. 1997, 94, 6185–6190.
- (27) Yu, Z.; Mao, H. Chem. Rec. 2013, 13, 102-116.
- (28) Dhakal, S.; Cui, Y.; Koirala, D.; Ghimire, C.; Kushwaha, S.; Yu, Z.; Yangyuoru, P. M.; Mao, H. *Nucleic Acids Res.* **2013**, *41*, 3915–3923.
- (29) Yurke, B.; Turberfield, A. J.; Mills, A. P.; Simmel, F. C.; Neumann, J. L. *Nature* **2000**, 406 (6796), 605–608.
- (30) Zhang, D. Y.; Seelig, G. Nat. Chem. 2011, 3 (2), 103-113.
- (31) Takamizawa, J.; Konishi, H.; Yanagisawa, K.; Tomida, S.; Osada, H.; Endoh, H.; Harano, T.; Yatabe, Y.; Nagino, M.; Nimura, Y.; Mitsudomi, T.; Takahashi, T. *Cancer Res.* **2004**, *64* (11), 3753–3756.
- (32) Woodside, M. T.; Behnke-Parks, W. M.; Larizadeh, K.; Travers, K.; Herschlag, D.; Block, S. M. *Proc. Natl. Acad. Sci. U. S. A.* **2006**, *103* (16), 6190–6195.
- (33) Vasudevan, S.; Tong, Y.; Steitz, J. A. Science **2007**, 318 (5858), 1931–1934.
- (34) Fu, H.; Tie, Y.; Xu, C.; Zhang, Z.; Zhu, J.; Shi, Y.; Jiang, H.; Sun, Z.; Zheng, X. FEBS Lett. **2005**, 579 (17), 3849–54.
- (35) Mitchell, P. S.; Parkin, R. K.; Kroh, E. M.; Fritz, B. R.; Wyman, S. K.; Pogosova-Agadjanyan, E. L.; Peterson, A.; Noteboom, J.; O'Briant, K. C.; Allen, A.; Lin, D. W.; Urban, N.; Drescher, C. W.; Knudsen, B. S.; Stirewalt, D. L.; Gentleman, R.; Vessella, R. L.; Nelson, P. S.; Martin, D. B.; Tewari, M. *Proc. Natl. Acad. Sci. U. S. A.* **2008**, *105* (30), 10513–10518.
- (36) Liu, R.; Zhang, C.; Hu, Z.; Li, G.; Wang, C.; Yang, C.; Huang, D.; Chen, X.; Zhang, H.; Zhuang, R.; Deng, T.; Liu, H.; Yin, J.; Wang, S.; Zen, K.; Ba, Y.; Zhang, C.-Y. Eur. J. Cancer **2011**, 47 (5), 784–791.
- (37) Koirala, D.; Yu, Z.; Dhakal, S.; Mao, H. J. Am. Chem. Soc. 2011, 133 (26), 9988–9991.
- (38) Lagos-Quintana, M.; Rauhut, R.; Lendeckel, W.; Tuschl, T. Science 2001, 294 (5543), 853-858.
- (39) Lewis, B. P.; Shih, I. h.; Jones-Rhoades, M. W.; Bartel, D. P.; Burge, C. B. *Cell* **2003**, *115* (7), 787–798.
- (40) Lu, Y.; Liu, J. Curr. Opin. Biotechnol. 2006, 17 (6), 580-588.
- (41) Dieckmann, T.; Fujikawa, E.; Xhao, X.; Szostak, J.; Feigon, J. J. Cell. Biochem. 1995, 59, 56.

(42) Daniels, D. L.; Schroeder, J. L.; Szybalski, W.; Sanger, F.; Coulson, A. R.; Hong, G. F.; Hill, D. F.; Petersen, G. B.; Blattner, F. R. APPENDIX II Complete Annotated Lambda Sequence; Cold Spring Harbor. 1983.

(43) Chen, M.; Hsinchu; Shen, J. DIGITIMES 2018, na.